• Original Paper •

Differences between Convective and Stratiform Precipitation Budgets in a Torrential Rainfall Event

Yongjie HUANG[1,3], Yaping WANG[1,3], and Xiaopeng CUI*[1,2,3]

[1]*Key Laboratory of Cloud-Precipitation Physics and Severe Storms, Institute of Atmospheric Physics, Chinese Academy of Sciences, Beijing 100029, China*

[2]*Collaborative Innovation Center on Forecast and Evaluation of Meteorological Disasters, Nanjing University of Information Science and Technology, Nanjing 210044, China*

[3]*University of Chinese Academy of Sciences, Beijing 100049, China*

ABSTRACT

Differences in rainfall budgets between convective and stratiform regions of a torrential rainfall event were investigated using high-resolution simulation data produced by the Weather Research and Forecasting (WRF) model. The convective and stratiform regions were reasonably separated by the radar-based convective–stratiform partitioning method, and the three-dimensional WRF-based precipitation equation combining water vapor and hydrometeor budgets was further used to analyze the rainfall budgets. The results showed that the magnitude of precipitation budget processes in the convective region was one order larger than that in the stratiform region. In convective/stratiform updraft regions, precipitation was mainly from the contribution of moisture-related processes, with a small negative contribution from cloud-related processes. In convective/stratiform downdraft regions, cloud-related processes played positive roles in precipitation, while moisture-related processes made a negative contribution. Moisture flux convergence played a dominant role in the moisture-related processes in convective or stratiform updraft regions, which was closely related to large-scale dynamics. Differences in cloud-related processes between convective and stratiform regions were more complex compared with those in moisture-related processes. Both liquid- and ice-phase microphysical processes were strong in convective/stratiform updraft regions, and ice-phase processes were dominant in convective/stratiform downdraft regions. There was strong net latent heating within almost the whole troposphere in updraft regions, especially in the convective updraft region, while the net latent heating (cooling) mainly existed above (below) the zero-layer in convective/stratiform downdraft regions.

Key words: convective rainfall, stratiform rainfall, precipitation budget, updraft region, downdraft region

Article Highlights:

• Precipitation budget processes in the convective region were one order of magnitude larger than those in the stratiform region.
• Moisture-related processes mainly contributed to precipitation in updraft regions, while cloud-related processes dominated in downdraft regions.
• Both liquid- and ice-phase microphysical processes were strong in updraft regions, and ice-phase processes were dominant in downdraft regions.

---

1. Introduction

Generally, precipitation can be classified into two types (i.e., convective and stratiform precipitation) based on differences in the nature of precipitation (Houze, 2014). Convective precipitation particles form in the active updraft of cumulus and cumulonimbus clouds, grow primarily by the coalescence and/or riming of cloud droplets, and fall out near their originating updraft (American Meteorological Society Glossary of Meteorology, http://glossary.ametsoc.org/wiki/Convective_precipitation). Whereas, stratiform precipitation generally falls from nimbostratus clouds in which vertical motions are weak and precipitation particles grow mainly because of water vapor condensation and deposition. In well-developed stratiform precipitation, there is always a bright

---

* Corresponding author: Xiaopeng CUI

  Email: xpcui@mail.iap.ac.cn

band on radar echo, which is associated with precipitating ice particles falling and growing by water vapor deposition, aggregating to form large snowflakes, and then melting (http://glossary.ametsoc.org/wiki/Stratiform_precipitation_area). As two basic types of precipitation, convective and stratiform precipitation have remarkable differences between each other (Houze, 2014). A strong ascending motion throughout the troposphere is always observed in convective regions, while there is a relatively uniform weak ascending or descending velocity in stratiform regions (Houze, 1989; Sui et al., 1994; Xu, 1995; Sui et al., 2007; Ahmed and Schumacher, 2015). Many studies (e.g., Morrison et al., 2009; Luo et al., 2010; Penide et al., 2013; Wu et al., 2013; Thurai et al., 2016) have indicated that distinct differences exist in the cloud microphysics between convective and stratiform regions. Wu et al. (2013) investigated convective and stratiform characteristics in two high precipitation squall line events and found that graupel and hail resided largely in the convective region, while cloud ice and snow resided largely in the stratiform region. Yang and Smith (2000) analyzed the vertical structures of averaged latent heat releases for convective and stratiform regions derived from SSM/I measurements, and found that the latent heating is much stronger for convective precipitation than stratiform precipitation, with maxima of $8.3°$ d^{-1} and $4.2°$ d^{-1}, respectively. Houze (1997) summarized the characteristic profiles of latent heat releases in convective and stratiform regions of tropical precipitation: net upward mass transport produces net latent heating at all levels in convective regions, while net cooling occurs as a result of melting and evaporation at mid to low levels in stratiform regions. Based on the considerable differences in the distributions of latent heat releases between convective and stratiform regions, convective–stratiform heating algorithms have been developed to estimate heating profiles and four-dimensional latent heating structures (Tao et al., 2000, 2001, 2010).

There are large differences in precipitation between convective and stratiform regions because of their obviously different dynamics, thermodynamics and cloud microphysics (Houze, 1982, 2014; Morrison et al., 2009; Penide et al., 2013; Rulfová and Kyselý, 2013). Houze (2014) indicated that convective precipitation falls from dynamically active cumulus and cumulonimbus clouds, while stratiform precipitation falls from nimbostratus clouds. Convective precipitation rates are often larger than stratiform precipitation rates, but with smaller coverage (Wu et al., 2013). Based on ground-based radar and satellite observations, Ahmed and Schumacher (2015) found that empirical relationships between precipitation and column moisture are markedly different in convective and stratiform rain systems. Therefore, it is very important to treat convective and stratiform precipitation separately in rainfall process analysis. Based on the abovementioned different features between convective and stratiform rainfall regions, many methods have been proposed to divide precipitation into convective and stratiform components, such as methods based on rain rate (Churchill and Houze, 1984; Tao et al., 1993; Sui et al., 1994), radar reflectivity (Steiner et al., 1995; Yang et al., 2013), and vertical motion (Xu,

1995). Based on the different heating profiles between convective and stratiform regions, Huang et al. (2018) developed a new scheme to assimilate radar reflectivity data into numerical models, which showed good forecasting performance.

Precipitation is a result of interactions among dynamics, thermodynamics and cloud microphysics (Huang et al., 2016b). In order to understand the physical processes and mechanisms in surface precipitation thoroughly, Gao et al. (2005) combined the water vapor budget with the cloud hydrometeor budget to derive a diagnostic equation—a surface rainfall budget equation in a two-dimensional cloud-resolving model framework (hereinafter 2D CRM-based surface rainfall budget equation). The equation has been widely applied to quantitatively diagnosing a variety of precipitation budget processes (Cui and Li, 2006; Li, 2006; Wang et al., 2007; Cui, 2008; Cui and Li, 2009; Cui and Li, 2009; Gao et al., 2009; Gao and Li, 2010; Wang et al., 2010; Cui and Li, 2011; Shen et al., 2011). Huang et al. (2016b) extended the 2D CRM-based surface rainfall equation to the 3D WRF-based precipitation equation. They used the newly obtained equation to examine the rainfall budget of a torrential rainfall event in Sichuan, China, and found that the moisture-related processes (especially moisture flux convergence) dominated the torrential rain event, while the cloud-related processes played smaller but by no means negligible roles (Huang et al., 2016b).

However, Huang et al. (2016b) performed an area-averaged analysis of the rainfall region. The different budget characteristics of the convective and stratiform precipitation were not investigated. As stated above, convective and stratiform regions show significant differences in precipitation processes, so it is extremely necessary to investigate precipitation budgets in convective and stratiform regions separately. In this study, following Huang et al. (2016b), precipitation was further partitioned into convective and stratiform components to investigate the differences in precipitation budgets between convective and stratiform rainfall. Section 2 introduces the model setup and method. The analyses of convective–stratiform rainfall budgets are presented in section 3. Conclusions and discussion are given in section 4.

2. Model and method

2.1. *Model setup*

A torrential rainfall event occurred during 19–20 August 2010 on the western edge of the Sichuan Basin, China, causing serious debris flows. Li et al. (2014) simulated this torrential rain event successfully using the Weather Research and Forecasting (WRF) model. The model was integrated from 0200 LST (Local Standard Time, UTC + 8 h) 18 August to 0800 LST 20 August 2010 (54 hours) using three one-way nesting domains with horizontal grid spacings of 27, 9, and 3 km, respectively. The grid points in the west–east and south–north directions were 268×245, 583×292, and 790×610 for the three domains, respectively. The model domains used 30 vertical levels up to 50 hPa. In the 3-km

resolution domain, the cumulus convective parameterization scheme was not activated and only the cloud microphysical parameterization scheme—the Milbrandt double-moment scheme (Milbrandt and Yau, 2005a, b)—was used. The Milbrandt scheme includes seven water species, i.e., water vapor (Q_v), cloud water (Q_c), rain water (Q_r), cloud ice (Q_i), snow (Q_s), graupel (Q_g), and hail (Q_h). By using this bulk microphysics scheme, Milbrandt et al. (2010) successfully reproduced an orographic precipitation event during IMPROVE-2 (the second Improvement of Microphysical Parameterization through Observational Verification Experiment). Huang and Cui (2015a) and Huang et al. (2016a) utilized similar WRF model setups as Li et al. (2014) to investigate the dominant cloud microphysical processes and cloud microphysical differences with precipitation intensity in the above torrential rain event. By using the 3D WRF-based precipitation budget equation, Huang et al. (2016b) studied the physical processes and mechanisms associated with the heavy rainfall event. Referring to the aforementioned studies (Li et al., 2014; Huang

and Cui, 2015a; Huang et al., 2016a, b), the simulation data were evaluated in the aspects of large-scale circulation, precipitation, and cloud structures by using the available data from reanalysis, automatic weather stations, rain gauges, and radar observation. The simulated radar composite reflectivity resembled the observed one, especially the distribution of relatively strong radar echo bands (Fig. 1). The observed radar echo covered a relatively smaller range because of the radar detection range and the terrain blocking of the Tibetan Plateau. Obvious convective and stratiform regions existed in this event, based on the radar reflectivity distribution (Fig. 1). Therefore, this torrential rain event was selected again to investigate the differences in precipitation budgets between convective and stratiform precipitation in this study. For more details of the model setups and verification, please refer to Li et al. (2014), Huang and Cui (2015a), and Huang et al. (2016a, b). Simulation data in the 3-km resolution domain from 0800 LST 18 August to 0800 LST 20 August 2010 (48 hours, discarding the first six hours of data used for model
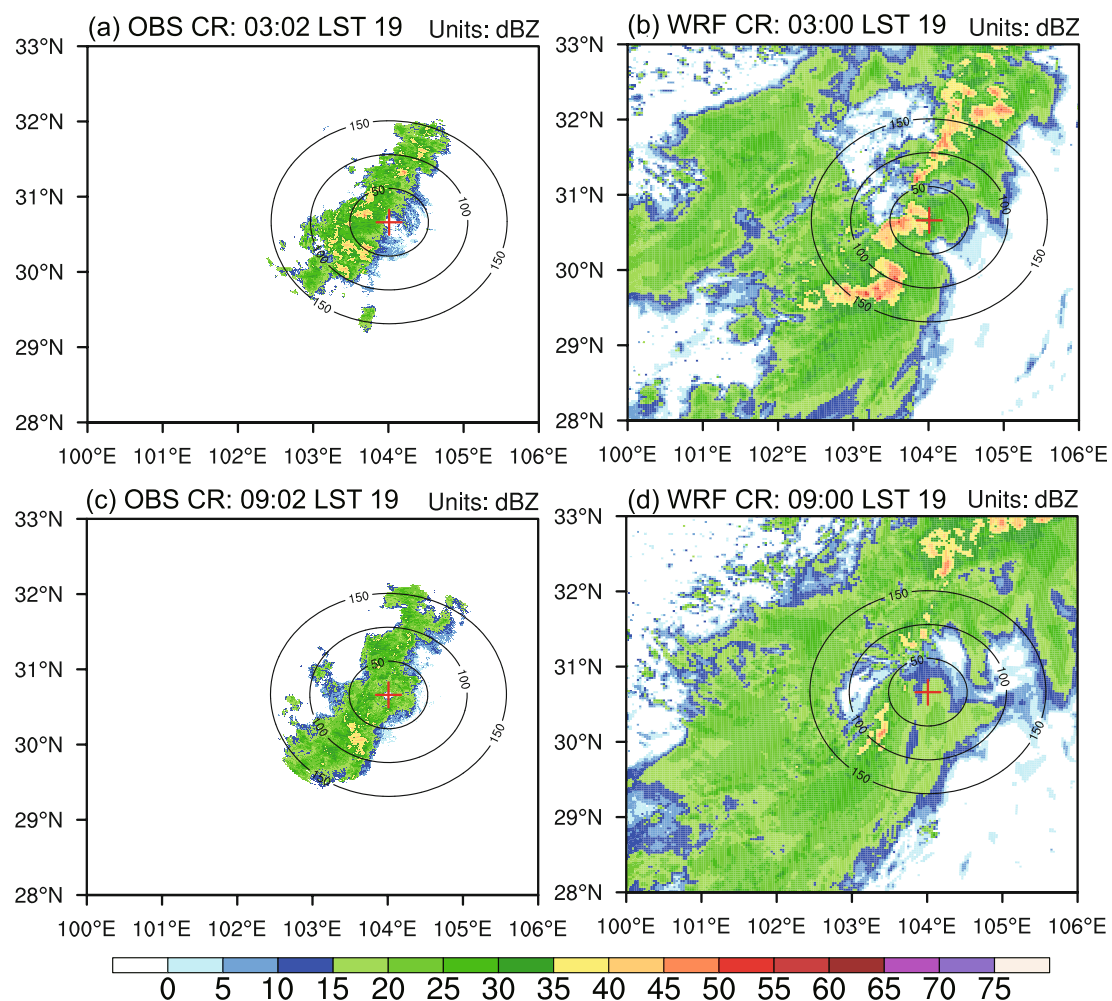

Fig. 1. The (a, c) observed and (b, d) simulated radar composite reflectivity (color-shaded; units: dBZ). The times for (a, b) are 0302 and 0300 LST 19 August 2010, respectively. The times for (c, d) are 0902 and 0900 LST 19 August 2010, respectively. The red plus sign represents the location of Chengdu radar station. Black contours display the distance from Chengdu radar station.

spin-up) were used for statistical analysis in this study.

2.2. *Convective and stratiform rainfall partitioning method*

Based on differences in the nature of precipitation, rainfall can be classified roughly into convective and stratiform rain regions, which present different characteristics in dynamics, thermodynamics, and cloud microphysics. Therefore, it is worthwhile to investigate differences in precipitation budgets between convective and stratiform regions.

There are several different convective–stratiform rainfall partitioning methods proposed in previous studies, such as methods based on surface rainfall rate (Churchill and Houze, 1984), radar reflectivity (Steiner et al., 1995), and vertical motion (Xu, 1995). The convective–stratiform rainfall partitioning method used in this study is a method based on radar reflectivity developed by Steiner et al. (1995), with some of the thresholds (e.g., reflectivity factor thresholds, background radius) from Feng et al. (2011). Wu et al. (2013) used the same partitioning algorithm to investigate characteristics of precipitation, wind, and microphysical fields in convective and stratiform regions of two high precipitation squall line events, and demonstrated that the algorithm can reasonably identify the WRF-simulated fields in both convective and stratiform regions. The detailed partitioning steps are as follows:

(1) Calculate the equivalent radar reflectivity factor (Z_e) in units of dBZ by using the WRF model output data at 3 km above mean sea level (MSL), which is sufficiently below the 0°C level [~5.5 km above MSL; Figs. 7–9 in this paper; also see Fig. 4 in Huang and Cui (2015a) and Fig. 3 in Huang et al. (2016a)] to minimize bright band contamination. Model grid points whose Z_e are larger than 43 dBZ (Feng et al., 2011) are identified as convective cores directly.

(2) If the difference between a grid's Z_e and its background reflectivity factor [Z_{bg}; averaged Z_e with a 6-km radius centered on the grid (Feng et al., 2011)] exceeds its background intensity threshold value (determined by a function of Z_{bg}), it is assigned as a convective grid.

(3) Through steps (1) and (2), convective centers are identified, and their surrounding grid points within a convective radius (determined by a function of Z_{bg}) around the convective centers are also assigned as convective grids.

(4) As for the rest of the grid points that are not identified as convective grids, if their Z_e exceeds 10 dBZ (Feng et al., 2011), they are designated as stratiform grids.

(5) Finally, the remaining grid points that are not identified as either convective or stratiform grids are assigned as non-classified grids, which are not included in the statistical range (since this study focuses on differences between convective and stratiform rainfall regions).

2.3. *3D WRF-based precipitation budget equation*

Following Gao et al. (2005) and Huang et al. (2016b), the surface precipitation rate (P_S) can be simply expressed as

$$P_S = Q_{WV} + Q_{CM}, \tag{1}$$

where Q_{WV} represents change rates of moisture-related processes (including the water vapor local change rate, moisture flux convergence rate, moisture diffusion rate, and surface evaporation rate) and Q_{CM} represents change rates of cloud-related processes (including the local change rate, flux convergence rate, and diffusion rate of hydrometeors). Equation (1) can be interpreted as follows: Water vapor must be converted to cloud hydrometeors first before it can contribute to precipitation. If $Q_{WV} > P_S$ (i.e., $Q_{WV} > 0$ and $Q_{CM} < 0$), it indicates that water vapor collected by moisture-related processes is not only used for precipitation but also to support cloud-related processes (e.g., increasing the content of cloud hydrometeors, cloud hydrometeor divergence, etc.). On the contrary, if $Q_{WV} < P_S$ (i.e., $Q_{WV} > 0$ and $Q_{CM} > 0$), it implies that water vapor collected by moisture-related processes is not enough for surface precipitation, and the remaining amount ($P_S - Q_{WV}$) needs the supplement of cloud hydrometeors that already exist in the region. Thus, the surface precipitation budget equation, which connects the water vapor budget and cloud hydrometeor budget directly to the surface precipitation rate, is very helpful to quantitatively diagnose the role of each process in the final surface precipitation.

The change rates of moisture-related processes (Q_{WV}) can be further broken down into four components, i.e.,

$$Q_{WV} = Q_{WVL} + Q_{WVA} + Q_{WVD} + Q_{WVE}. \tag{2}$$

Similarly, the change rates of cloud-related processes (Q_{CM}) include six components, i.e.,

$$Q_{CM} = Q_{CLL} + Q_{CLA} + Q_{CLD} + Q_{CIL} + Q_{CIA} + Q_{CID}. \tag{3}$$

All these terms are vertically integrated. The meaning of each term can be found in Table 1, and the specific expression of each term can be found in Huang et al. (2016b). In this study, each term in the 3D WRF-based precipitation budget equation was output directly from the WRF model Huang et al. (2016b).

Table 1. The meaning of each term in the 3D WRF-based precipitation budget equation.

Term	Physical meaning
P_S	Surface precipitation rate
Q_{WV}	Net change rate of moisture-related processes
Q_{CM}	Net change rate of cloud-related processes
Q_{WVL}	Water vapor local change rate (local atmosphere drying or moistening)
Q_{WVA}	Moisture flux convergence rate
Q_{WVD}	Moisture diffusion rate
Q_{WVE}	Surface evaporation rate
Q_{CLL}	Local change rate of liquid-phase hydrometeors (cloud water and rain water)
Q_{CLA}	Liquid-phase hydrometeor flux convergence rate
Q_{CLD}	Diffusion rate of liquid-phase hydrometeors
Q_{CIL}	Local change rate of ice-phase hydrometeors (cloud ice, snow, graupel and hail)
Q_{CIA}	Ice-phase hydrometeor flux convergence rate
Q_{CID}	Diffusion rate of ice-phase hydrometeors

3. Results

3.1. *Distribution and evolution of convective and strati-form rain*

Precipitation classification results during 1000 LST 18 to 0800 LST 20 August 2010 at 2-h intervals are shown in Fig. 2. During the early precipitation period (1000–2000 LST 18 August 2010), both convective and stratiform rainfall regions were relatively small and scattered. With the precipitation system development, convective regions (red areas; CC) began to consolidate, and were surrounded by stratiform regions (blue areas; SR). Then, both convective and stratiform areas were expanding. Convective areas began to decrease at 0600 LST 19 August, while stratiform rain remained widespread. During the latter precipitation period, stratiform rain coverage was also shrinking, and the precipitation system gradu-
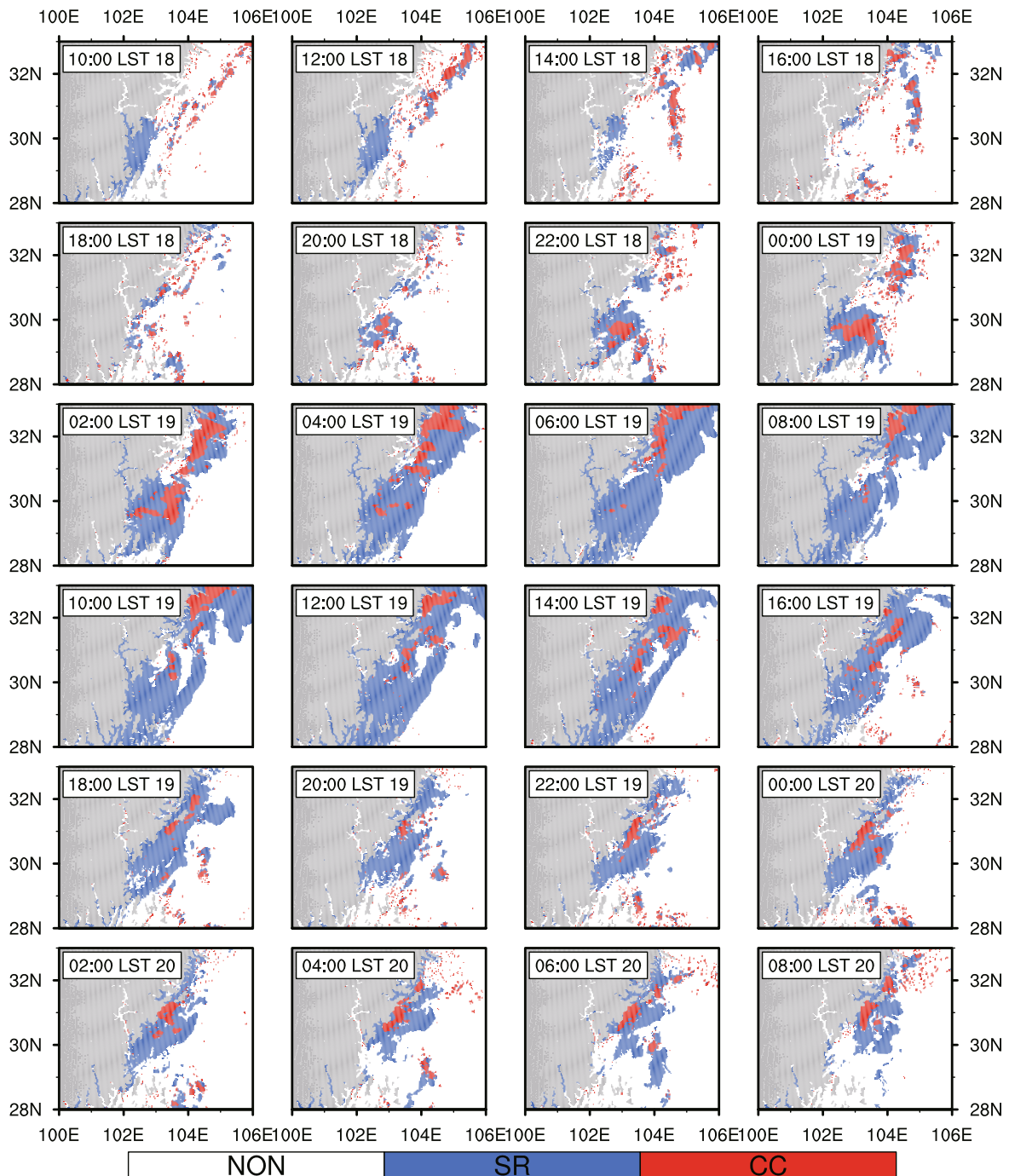

Fig. 2. Distribution of different precipitation types from 1000 LST 18 to 0800 LST 20 August 2010 (2-h intervals). Blue shaded areas (SR): stratiform rain; red shaded areas (CC): convective rain; white shaded areas (NON): non-classified regions; gray shaded areas represent no radar reflectivity data at 3 km above sea level because of elevated terrain.

ally weakened and dissipated.

In order to investigate the evolution of convective and stratiform coverage and precipitation intensity more clearly, time series of area coverages and surface precipitation rates for convective and stratiform regions from 0800 LST 18 to 0800 LST 20 August 2010 are shown in Fig. 3. During the whole period (Fig. 3), the percentages of convective areal coverage against the area of the study domain (excluding grids with no radar data; gray areas in Fig. 2) were basically below 10%, while stratiform coverage was substantially larger than 10%, and its maximum could reach 45%. On average for the whole period, convective areal coverage was 5.48%, while stratiform coverage was 22.29%, which was around four times as much as the convective coverage (Fig. 3). As for averaged surface precipitation rates for convective and stratiform regions, rain rates in convective regions had obvious fluctuations with multiple peaks, and reached its maximum (~13 mm h^{-1}) at 0100 LST 19 August, while rain rates in stratiform regions were relatively smoother and distinctly smaller, basically around 1 mm h^{-1} (Fig. 3). The time-averaged precipitation rate for stratiform rain was 1.07 mm h^{-1}, while it was 7.22 mm h^{-1} for convective rain, which was ~ 5.75 times larger than that of stratiform region.

The characteristics described above show the typical differences between convective and stratiform rain (Wu et al., 2013). Convective rain has smaller areal coverage, a larger surface rain rate, and is faster changing, while stratiform rain has larger areal coverage, a smaller surface rain rate, and is more gently changing. This illustrates that the convective–stratiform classification result in this study is reasonable.

3.2. *Vertical velocity characteristics and updraft/downdraft identification*

To reveal the bulk vertical velocity characteristics, Contoured-Frequency-with-Altitude Diagrams (CFADs) Yuter and Houze (1995) of vertical velocity in convective
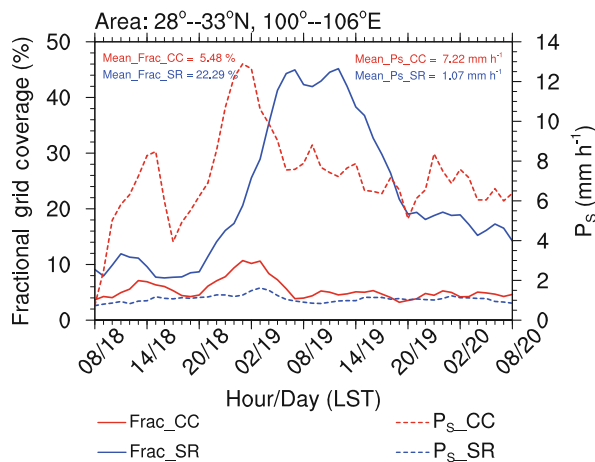

Fig. 3. Area coverage (solid lines; units: %) and surface precipitation rate (dashed lines; units: mm h^{-1}) averaged in convective (red line) and stratiform (blue line) regions from 0800 LST 18 to 0800 LST 20 August 2010.
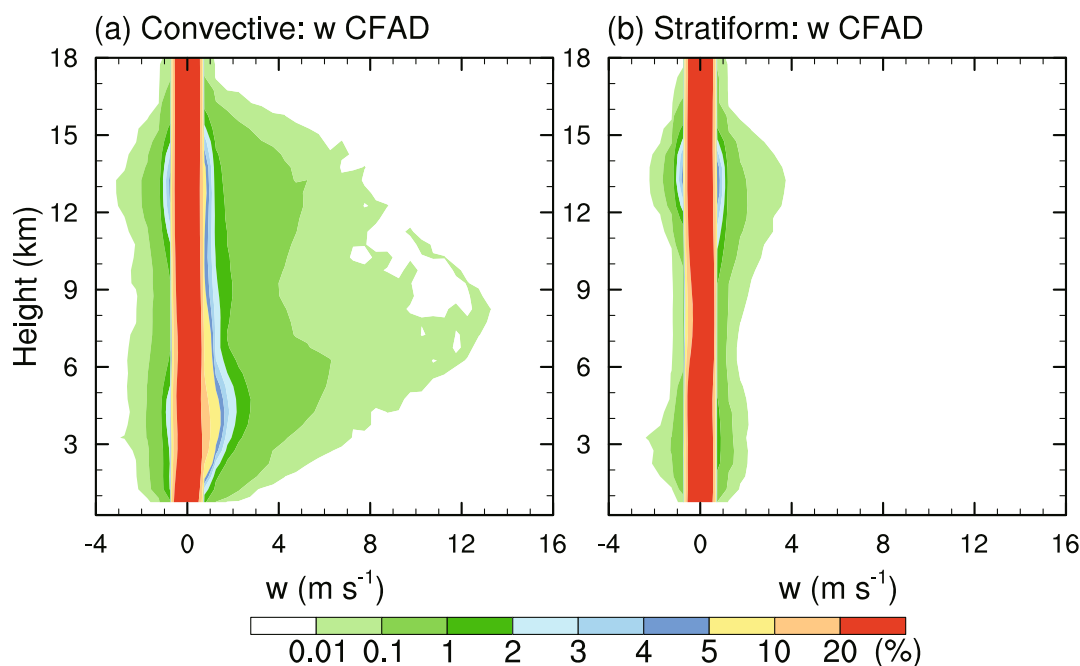
and stratiform regions during 0800 LST 18 to 0800 LST 20 August 2010 are shown in Fig. 4. From Fig. 4, the updrafts in the convective region were much stronger than those in the stratiform region (almost all the vertical velocities of stratiform girds were smaller than 4 m s^{-1}), and the maximum vertical ascending motion in the convective region was located at ~ 8 km above MSL. The downdrafts in the convective region were also a little stronger than those in the stratiform region, while their magnitudes were similar (Fig. 4). These distinguishable differences are also typical between convective and stratiform regions, demonstrating once again the convective–stratiform classification result in this study is reasonable. The distribution of CFADs of vertical velocities in convective and stratiform regions in this study is similar to that in reported in a previous study by Wu et al. (2013).

In previous studies (Houze, 1977, 1989; Zipser, 1977; Mrowiec et al., 2012), both updrafts and downdrafts have been found in convective and stratiform regions, which were also found in this study (Fig. 4). The updraft and downdraft regions may have different physical processes. Therefore, the convective and stratiform regions were further separated into updraft and downdraft regions. In this study, the vertically averaged mass flux was used to identify the updraft and downdraft columns in convective and stratiform regions, respectively. The vertically averaged mass flux is defined as $\overline{F_M} = \int_{z_s}^{z_t} \rho w dz/(z_t - z_s)$, where ρ is air density, w is vertical velocity, and z_s and z_t are the height above MSL of the model surface and top, respectively. The column where $\overline{F_M} > 0$ is identified as the updraft column, and the column where $\overline{F_M} < 0$ is identified as the downdraft column. To filter out the small and insignificant vertical motions that would dominate the mean conditions, only the data larger than the 10th percentile were used for statistical analysis in this study (Mrowiec et al., 2012).

Figure 5 shows vertical profiles of averaged vertical velocity in the convective updraft, convective downdraft, stratiform updraft, and stratiform downdraft regions during 0800 LST 18 to 0800 LST 20 August 2010. The averaged vertical velocity in the convective updraft region was much stronger than that in the stratiform updraft region. The averaged vertical velocity in the convective updraft region was larger than 0.15 m s^{-1} from ~2 to ~13 km, with a maximum over 0.5 m s^{-1} at ~4 km above MSL, while it was less than 0.15 m s^{-1} in the stratiform updraft region (Fig. 5). The magnitudes of downdrafts in the convective and stratiform regions were similar, but the downdraft in the convective region was a little stronger (weaker) than that in the stratiform region below (above) ~12 km (Fig. 5). The identification of updrafts and downdrafts in convective and stratiform regions is relatively reasonable (Mrowiec et al., 2012; Kumar et al., 2016).

3.3. *Precipitation budget*

In order to compare the differences in precipitation budgets between convective and stratiform regions, the averaged P_S, Q_{WV}, Q_{CM}, Q_{WVL}, Q_{WVA}, Q_{WVD}, Q_{WVE}, Q_{CLL}, Q_{CLA}, Q_{CLD}, Q_{CIL}, Q_{CIA}, and Q_{CID} in the updraft and downdraft

Fig. 4. Contoured-frequency-with-altitude diagrams (CFADs) for vertical velocity in (a) convective and (b) stratiform regions within (28°–33°N, 100°–106°E) during 0800 LST 18 to 0800 LST 20 August 2010.
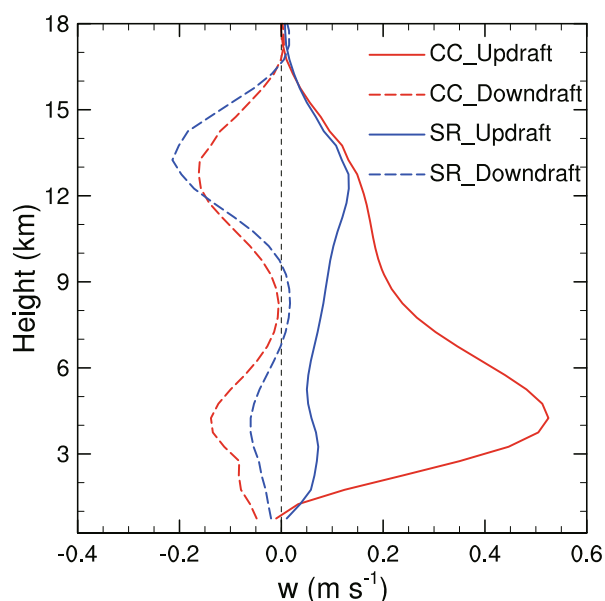

Fig. 5. Vertical profiles of averaged vertical velocity in convective updraft (red solid curve), convective downdraft (red dashed curve), stratiform updraft (blue solid curve), and stratiform downdraft (blue dashed curve) regions within (28°–33°N, 100°–106°E) during 0800 LST 18 to 0800 LST 20 August 2010.

regions of the convective and stratiform regions within (28°–33°N, 100°–106°E) during 0800 LST 18 to 0800 LST 20 August 2010 are shown in Fig. 6. The magnitudes of all these terms in the convective region were one order larger than

those in the stratiform region (Fig. 6). In the convective region, the averaged precipitation rate (P_S) could reach 9 and 3 mm h^{-1} in the updraft and downdraft regions, respectively (Fig. 6a). Plus, they were only 1.2 and 0.8 mm h^{-1} in the updrafts and downdrafts of the stratiform region, respectively (Fig. 6b). However, the main contribution terms to P_S in the updraft or downdraft regions were similar between the convective and stratiform regions. In the convective or stratiform updraft regions, Q_{WV} was larger than P_S, and Q_{CM} showed negative values (Fig. 6). This implies that, in updraft regions, precipitation mainly results from the combination of the positive contribution of Q_{WV} and the small negative contribution of Q_{CM}. In the convective or stratiform downdraft regions, Q_{WV} was negative, and Q_{CM} was positive and larger than P_S (Fig. 6), indicating that Q_{CM} is the contribution term to P_S in downdraft regions.

Further analysis of each term within the Q_{WV} showed that, in either convective or stratiform updraft regions, moisture flux convergence rates (Q_{WVA}) played a dominant role in the change rate of moisture-related processes, which was the main reason that moisture-related processes contributed significantly to precipitation in the convective or stratiform updraft regions. Q_{WVA} was much larger in the convective updraft region than in the stratiform updraft region (Fig. 6), because of the distinct differences in vertical ascending motions between them (Fig. 5). In convective or stratiform updraft regions, the water vapor local change rate made a negative contribution ($Q_{WVL} < 0$) to precipitation, corresponding to the effect of local atmospheric moistening processes (water vapor content increasing and the local atmosphere moistening) (Fig. 6). In convective or stratiform downdraft regions, Q_{WVA}
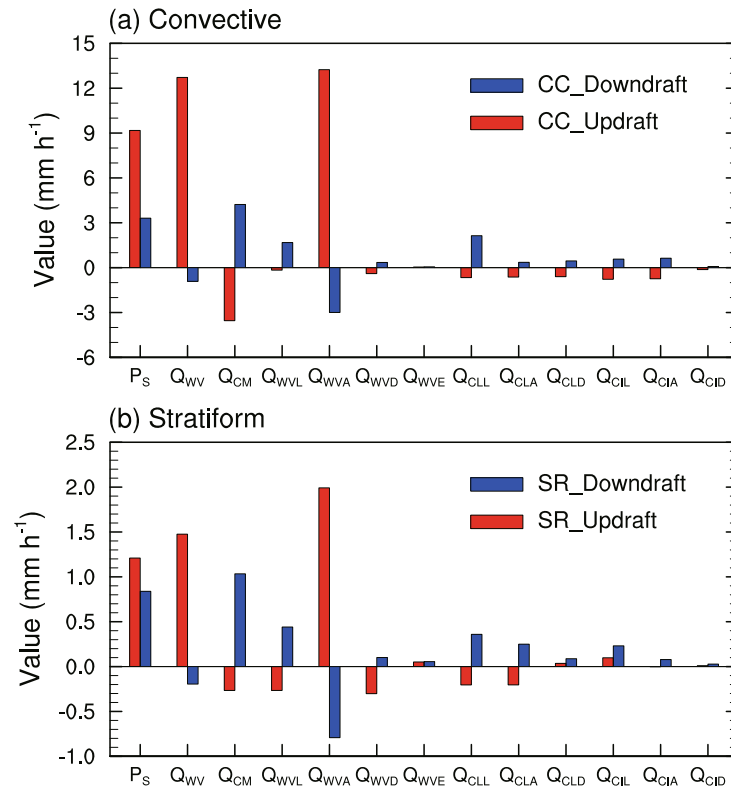
Fig. 6. Averaged P_S, Q_{WV}, Q_{CM}, Q_{WVL}, Q_{WVA}, Q_{WVD}, Q_{WVE}, Q_{CLL}, Q_{CLA}, Q_{CLD}, Q_{CIL}, Q_{CIA}, and Q_{CID} in updrafts (red bar) and downdrafts (blue bar) of (a) convective and (b) stratiform regions within (28°–33°N, 100°–106°E) during 0800 LST 18 to 0800 LST 20 August 2010. Units: mm h^{-1}.

was negative (moisture flux divergence) and Q_{WVL} was positive (water vapor content decreasing and the local atmosphere drying) with $|Q_{WVA}| > |Q_{WVL}|$, resulting in negative Q_{WV} in downdraft regions. The Q_{WVA} in downdraft regions was not so dominant as in updraft regions (Fig. 6), because of the differences in vertical velocity magnitudes between updraft and downdraft regions in the middle and lower troposphere (Fig. 5), where most water vapor exists. The surface evaporation rate (Q_{WVE}) played positive roles in moisture supply in both updraft and downdraft regions, but their magnitudes were overall quite small. Therefore, the differences in the water vapor budget between updraft and downdraft regions in both convective and stratiform regions were mainly caused by the big differences in Q_{WVA}.

The differences in cloud-related rates (Q_{CM}) between the updraft and downdraft regions in the convective and stratiform regions were more complex compared with those of moisture-related rates (Fig. 6). The total cloud-related rates in both convective and stratiform updraft regions were negative ($Q_{CM} < 0$); however, there were some differences in the sub-terms of Q_{CM}. All the sub-terms in the convective updraft region were negative, indicating that both liquid- and ice-phase cloud hydrometeors increased and diverged. In the stratiform updraft region, only Q_{CLL} and Q_{CLA} were negative, and the other sub-terms of Q_{CM} were relatively small

positive values, indicating that liquid-phase hydrometeors increased and divergence dominated. In convective or stratiform downdraft regions, Q_{CM} and all its sub-terms were positive (Fig. 6). Q_{CLL} dominated the hydrometeor budget in the convective downdraft region, indicating that the local change rate of liquid-phase hydrometeors (liquid-phase hydrometeors decreasing) is relatively important to the cloud budget and precipitation budget in this region. In the stratiform downdraft region, positive Q_{CLL}, Q_{CLA}, and Q_{CIL} (ice-phase hydrometeors decreasing) were almost equivalently important to the cloud budget and precipitation budget (Fig. 6).

3.4. *Hydrometeor distribution and cloud microphysical processes*

Though plenty of water vapor (same order of magnitude) existed in both the convective and stratiform regions (not shown), there were obvious differences in their cloud hydrometeors' vertical distributions (Fig. 7). There was much more cloud water, rain water, and graupel in the convective region (Figs. 7a and b), especially in the convective updraft region (Fig. 7a), than in the stratiform region (Figs. 7c and d). On the contrary, the contents of cloud ice and snow were a little larger in the stratiform than in the convective regions, especially the contents of snow (Fig. 7), consistent with Wu et al. (2013). The vertical profiles of the dominant
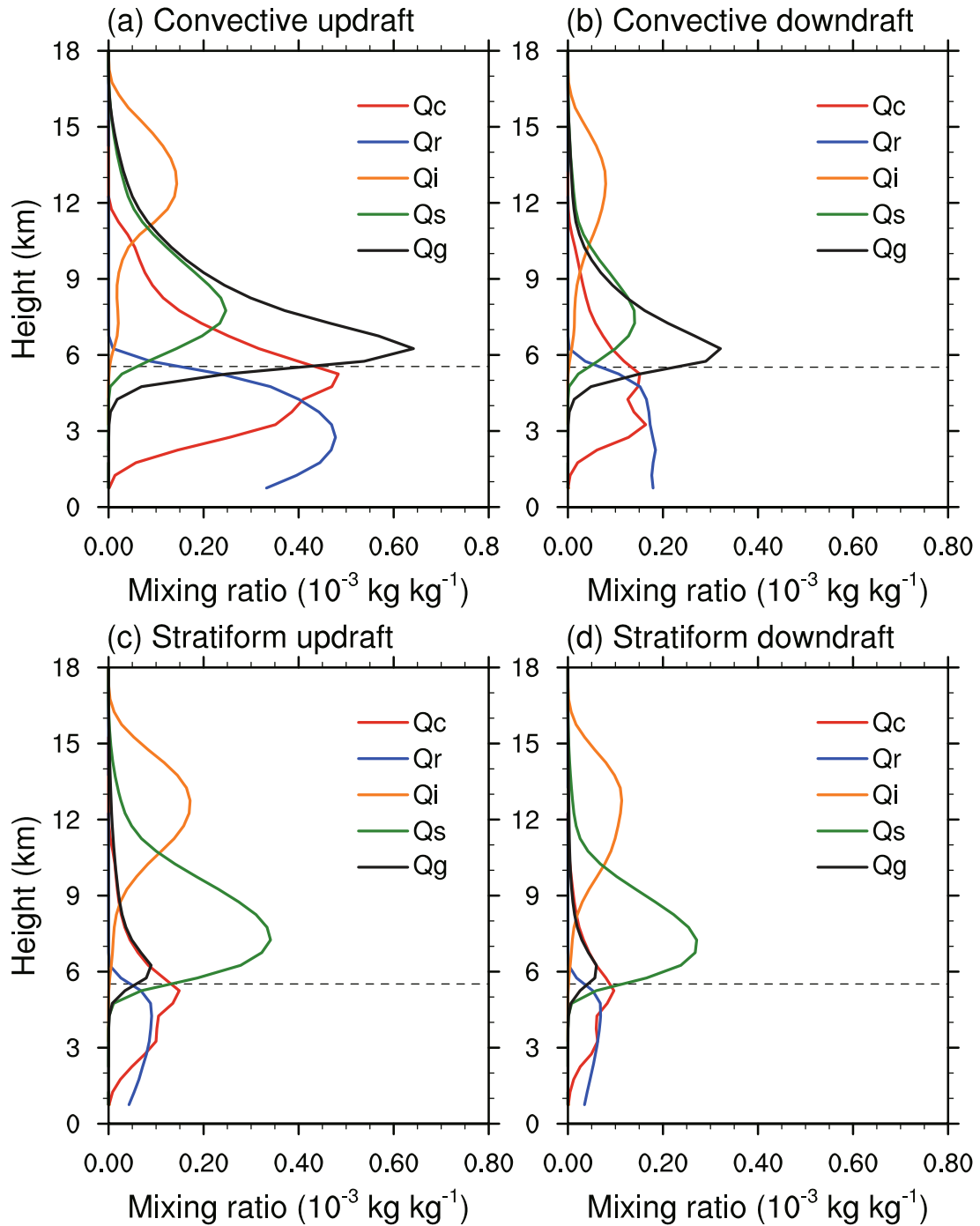
Fig. 7. Vertical profiles of averaged mixing ratios (units: 10^{-3} kg kg^{-1}) of cloud water (Q_c), rain water (Q_r), cloud ice (Q_i), snow (Q_s), and graupel (Q_g) in (a) convective updraft, (b) convective downdraft, (c) stratiform updraft, and (d) stratiform downdraft regions within (28°–33°N, 100°–106°E) during 0800 LST 18 to 0800 LST 20 August 2010. The horizontal dashed lines represent the height of 0°C.

microphysical processes revealed in Huang and Cui (2015a) and Huang et al. (2016a) are shown in Fig. 8. Water vapor condensation to cloud water (QVD$_{vc}$), accretion of cloud water by rain (QCL$_{cr}$), accretion of cloud water by graupel (QCL$_{cg}$), and melting of graupel to rain (QML$_{gr}$) were one order of magnitude stronger in the convective updraft region than in the stratiform updraft region, while melting of snow to rain (QML$_{sr}$) was slightly stronger in the stratiform updraft/downdraft regions than in the convective updraft/downdraft regions (Fig. 8). Plenty of water vapor from the much stronger moisture flux convergence rate (Q_{WVA}) in the convective updraft region (Fig. 6a) condensed into
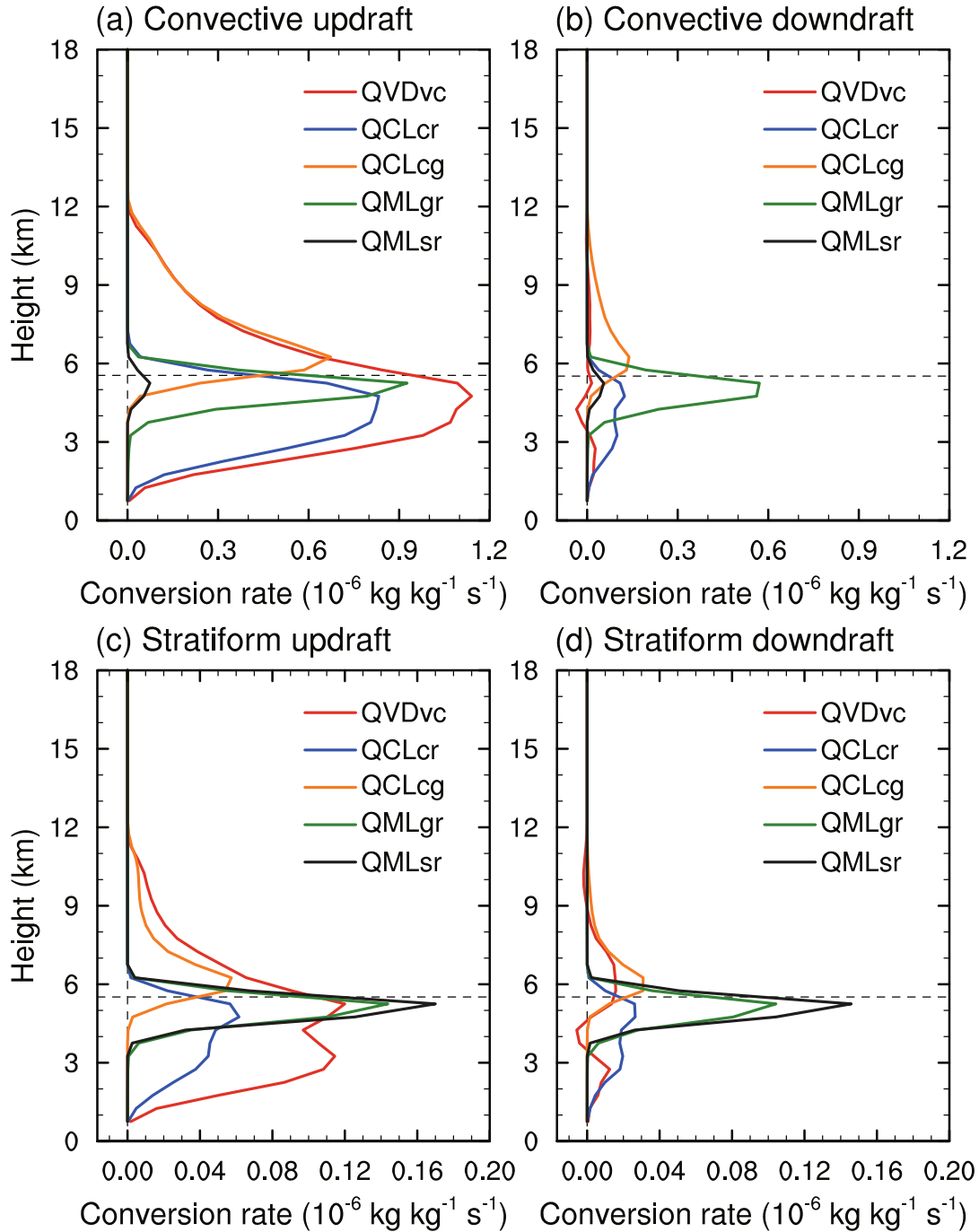
Fig. 8. Vertical profiles of averaged microphysical conversion rates (water vapor condensation to cloud water: $Q\mathrm{VD_{vc}}$; accretion of cloud water by rain to form rain: $Q\mathrm{CL_{cr}}$; accretion of cloud water by graupel to form graupel: $Q\mathrm{CL_{cg}}$; melting of graupel to rain: $Q\mathrm{ML_{gr}}$; melting of snow to rain: $Q\mathrm{ML_{sr}}$; units: 10^{-6} kg kg^{-1} s^{-1}) in (a) convective updraft, (b) convective downdraft, (c) stratiform updraft, and (d) stratiform downdraft regions within (28°–33°N, 100°–106°E) during 0800 LST 18 to 0800 LST 20 August 2010. The horizontal dashed lines represent the height of 0°C. The vertical dashed lines represent 0 kg kg^{-1} s^{-1}.

cloud water ($Q\mathrm{VD_{vc}}$, Fig. 8a). $Q\mathrm{VD_{vc}}$ was also one of the main terms in the stratiform updraft region (Fig. 8c). However, in both the convective and stratiform downdraft regions the Q_{WVA} was negative (Fig. 6) and the $Q\mathrm{VD_{vc}}$ was much weaker (Figs. 8b and d), which resulted in more cloud wa-

ter in the convective updraft region than in other regions (Fig. 7). The two main pathways for rain water generation [$Q\mathrm{VD_{vc}} \rightarrow Q\mathrm{CL_{cr}}$ and $Q\mathrm{VD_{vc}} \rightarrow Q\mathrm{CL_{cg}} \rightarrow Q\mathrm{ML_{gr}}$ (Huang and Cui, 2015a)] were both remarkable in the convective updraft region (Fig. 8a), but $Q\mathrm{ML_{gr}}$ was dominant in the

convective downdraft region (Fig. 8b). In stratiform regions (Figs. 8c and d), the melting processes (QML$_{gr}$ and QML$_{sr}$, especially the latter) dominated the rain water generation, especially in the stratiform downdraft region (Fig. 8d).

The microphysical processes with phase changes can heat the atmosphere with latent heat release or cool the atmo-

sphere with latent heat absorption. The heating processes include condensation, congelation, deposition, freezing, etc., and the cooling processes include evaporation, melting, and sublimation. Figure 9 shows vertical profiles of the microphysical latent heating/cooling rates in the convective updraft, convective downdraft, stratiform updraft, and strati-
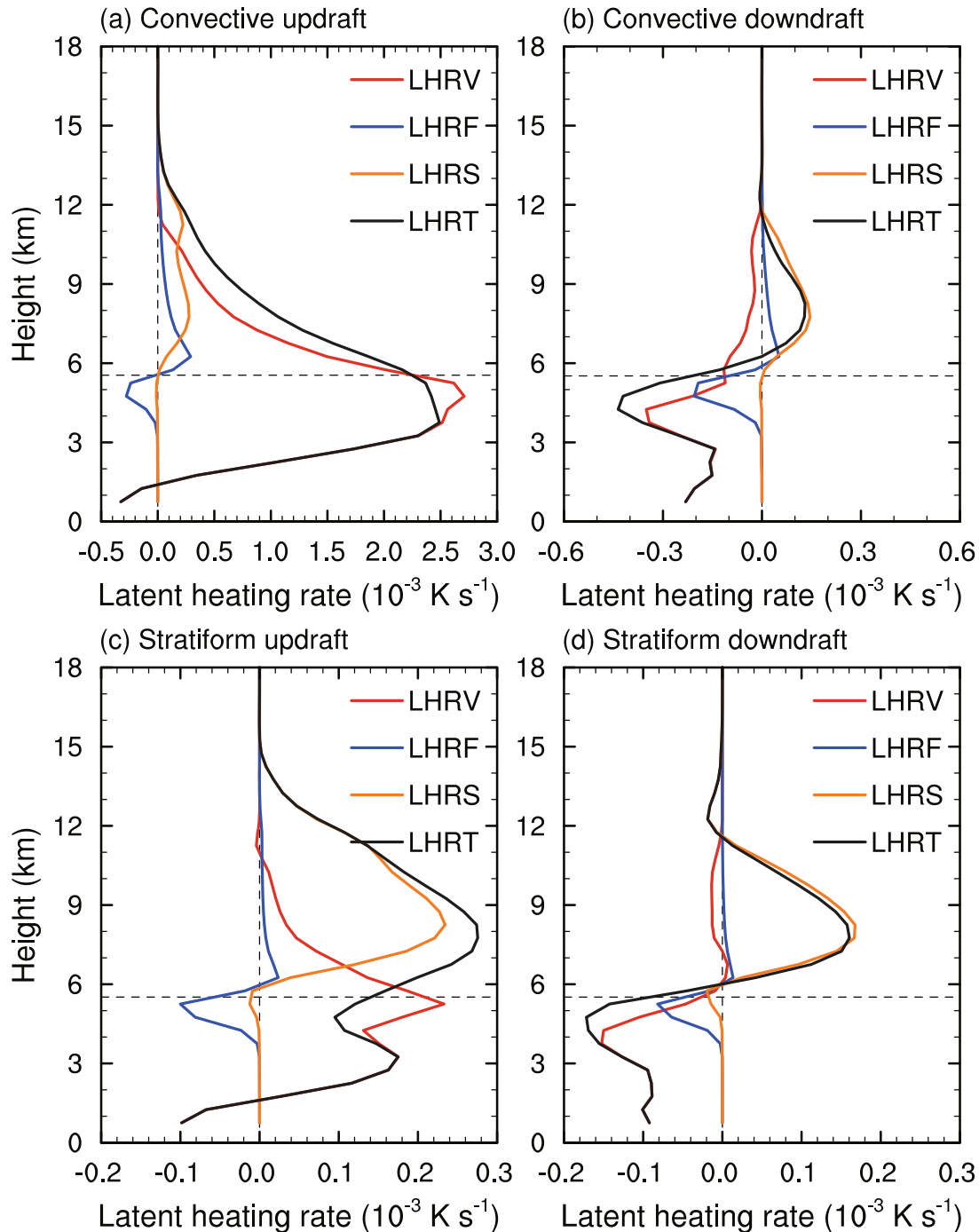

Fig. 9. Vertical profiles of averaged microphysical latent heating/cooling rates (latent heating/cooling rate of condensation/evaporation: LHRV; latent heating/cooling rate of freezing/melting: LHRF; latent heating/cooling rate of deposition/sublimation: LHRS; total latent heating/cooling rate: LHRT; units: 10^{-3} K s^{-1}) averaged in (a) convective updraft, (b) convective downdraft, (c) stratiform updraft, and (d) stratiform downdraft regions within (28°–33°N, 100°–106°E) during 0800 LST 18 to 0800 LST 20 August 2010. The horizontal dashed lines represent the height of 0°C. The vertical dashed lines represent 0 K s^{-1}.

form downdraft regions. The magnitude of the net latent heating rate in the convective updraft region was one order larger than those in the convective downdraft, stratiform updraft, and stratiform downdraft regions (Fig. 9). Owing to the distinct water vapor condensation in the convective updraft region (Fig. 8a), dominant condensation latent heat was released around the zero-layer (melting-layer) (positive LHRV in Fig. 9a), which is very important for the development of convective cloud systems as well as positive feedback to vertical upward motion. In the stratiform updraft region, latent heating mainly derived from condensation latent heating (positive LHRV) around the zero-layer and water vapor deposition heating (positive LHRS) above the zero-layer, which was partially balanced out by melting cooling (negative LHRF) just beneath the zero-layer (Fig. 9c). The latent heating/cooling profiles in the downdraft regions were more or less similar (Figs. 9b and d). In the downdraft regions, water vapor deposition heating (positive LHRS) dominated the net heating above the zero-layer, while both ice-phase hydrometeor melting cooling (negative LHRF) just beneath the zero-layer and rain water/cloud water evaporation cooling (negative LHRV) below the zero-layer played important roles in the net cooling there, and the latter was more distinct (Figs. 9b and d). Overall, there was strong net latent heating within almost the whole troposphere in the updraft regions, especially in the convective updraft region (Figs. 9a and c). In the downdraft regions, the net latent heating only existed above the zero-layer and the net latent cooling mainly existed beneath the zero-layer (Figs. 9b and d). The vertical distributions of latent heating/cooling rates were closely associated with those of vertical velocity (Fig. 5), indicating cloud development is closely related to the large-scale dynamics. These characteristics are similar to those reported in previous studies (Houze, 1997).

4. Conclusions and discussion

Owing to significant differences in dynamics, thermodynamics and microphysics between convective and stratiform precipitation, it is necessary to investigate the characteristics of precipitation budgets separately. In this study, the 3D WRF-based precipitation budget equation (Huang et al., 2016b) was used to examine the differences in precipitation budget processes between the convective and stratiform updraft/downdraft regions of a torrential rainfall event in Sichuan, China, using high-resolution simulation data produced by the WRF model. The major results can be summarized as follows:

(1) The typical differences in terms of areal coverage, surface rain rate, and vertical motion between the convective and stratiform regions indicated that the radar-based convective–stratiform partitioning method could classify the convective and stratiform regions reasonably.

(2) The magnitude of precipitation budget processes in the convective region was one order larger than that in the stratiform region. In the convective and stratiform updraft re-

gions, precipitation mainly resulted from the combination of the positive contribution of moisture-related processes and the small negative contribution of cloud-related processes. In the convective and stratiform downdraft regions, cloud-related processes played positive roles in precipitation, while moisture-related processes contributed negatively. Therefore, not only did distinct differences exist in precipitation budget processes between the convective and stratiform regions, but also between the updraft and downdraft regions.

(3) Moisture flux convergence played a dominant role in the moisture-related processes, either in the convective or stratiform updraft regions. However, it was much larger in the convective than stratiform updrafts, corresponding to the distinct differences in ascending motion between them. The differences in cloud-related processes between the convective and stratiform regions were more complex compared with those in moisture-related processes.

(4) There were significant differences in the cloud hydrometeor distribution, cloud microphysical processes, and latent heating/cooling profiles between the convective and stratiform updraft/downdraft regions, which was closely related to the large-scale vertical motion. Both liquid- and ice-phase processes were strong in the updraft regions, and ice-phase processes were dominant in the downdraft regions. In the updraft regions—especially in the convective updraft region—there was strong net latent heating within almost the whole troposphere, while in the downdraft regions net latent heating only existed above the zero-layer and net latent cooling mainly existed below the zero-layer.

Many studies have investigated the different characteristics of convective and stratiform precipitation from different perspectives, such as microphysics (Gamache, 1990; Cui et al., 2007; Grim et al., 2009; Niu et al., 2010), latent heating (Tao et al., 2010; Choudhury and Krishnan, 2011), precipitation fraction (Romatschke and Houze, 2011; Rapp et al., 2014), diurnal variation (Cui, 2008), characteristics of rain integral parameters (Sharma et al., 2009), and radar retrieval parameters (Penide et al., 2013; Bringi et al., 2015). However, to the best of our knowledge, the work reported in this paper may be the first attempt at investigating the differences in precipitation budgets separately in updraft and downdraft regions between convective and stratiform precipitation using the 3D WRF-based precipitation budget equation, which connects the large-scale water vapor budget and cloud hydrometeor budget directly to the surface rain rate, and could describe the dynamics and thermodynamics of the real atmosphere better (Huang et al., 2016b) compared with the 2D CRM-based surface rainfall budget equation (Gao et al., 2005). Also, we found that not only did distinct differences exist in the precipitation budgets between the convective and stratiform regions, but also the updraft and downdraft regions. Therefore, the results are very helpful towards thoroughly understanding the physical processes and mechanisms in different regions (updraft/downdraft) of convective and stratiform rainfall. Furthermore, it deepens our understanding of rainfall budget processes in the updraft/downdraft regions of different types of precipitation.

It should be noted that we also conducted sensitivity experiments with several different cloud microphysics schemes (i.e., the WSM6, WDM6, Thompson, and Morrison double-moment schemes). Although there were some differences in specific values of the results among the different sensitivity experiments, the main conclusions were consistent. It must be pointed out that, whilst only one event was analyzed here, previous studies have shown that the type of rainfall examined in this study is extremely common in summer in Sichuan (Huang and Cui, 2015a, b). Thus, the conclusions in this study may be more broadly representative. Nonetheless, more torrential rainfall cases featuring different types and other regions should be analyzed in future to add robustness and statistical significance to the present results.

REFERENCES

Ahmed, F., and C. Schumacher, 2015: Convective and stratiform components of the precipitation-moisture relationship. *Geophys. Res. Lett.*, **42**, 10 453–10 462, https://doi.org/10.1002/2015gl066957.

Bringi, V. N., L. Tolstoy, M. Thurai, and W. A. Petersen, 2015: Estimation of spatial correlation of drop size distribution parameters and rain rate using NASA's S-band polarimetric radar and 2D video disdrometer network: Two case studies from MC3E. *Journal of Hydrometeorology*, **16**, 1207–1221, https://doi.org/10.1175/JHM-D-14-0204.1.

Choudhury, A. D., and R. Krishnan, 2011: Dynamical response of the south Asian Monsoon trough to latent heating from stratiform and convective precipitation. *J. Atmos. Sci.*, **68**, 1347–1363, https://doi.org/10.1175/2011JAS3705.1.

Churchill, D. D., and R. A. Houze Jr., 1984: Mesoscale updraft magnitude and cloud-ice content deduced from the ice budget of the stratiform region of a tropical cloud cluster. *J. Atmos. Sci.* **41**, 1717–1725, https://doi.org/10.1175/1520-0469(1984)041<1717:mumaci>2.0.co;2.

Cui, X. P., 2008: A cloud-resolving modeling study of diurnal variations of tropical convective and stratiform rainfall. *J. Geophys. Res. Atmos.*, **113**, D02113, https://doi.org/10.1029/2007jd008990.

Cui, X. P., 2009: Quantitative diagnostic analysis of surface rainfall processes by surface rainfall equation. *Chinese Journal of Atmospheric Sciences*, **33**, 375–387, https://doi.org/10.3878/j.issn.1006-9895.2009.02.15. (in Chinese with English abstract)

Cui, X. P., and X. F. Li, 2006: Role of surface evaporation in surface rainfall processes. *J. Geophys. Res. Atmos.*, **111**, D17112, https://doi.org/10.1029/2005jd006876.

Cui, X. P., and X. F. Li, 2009: Diurnal responses of tropical convective and stratiform rainfall to diurnally varying sea surface temperature. *Meteor. Atmos. Phys.*, **104**, 53–61, https://doi.org/10.1007/s00703-008-0016-1.

Cui, X. P., and X. F. Li, 2011: A cloud-resolving modeling study of short-term surface rainfall processes. *Meteor. Atmos. Phys.* **111**, 1–11, https://doi.org/10.1007/s00703-010-0121-9.

Cui, X. P., Y. S. Zhou, and X. F. Li, 2007: Cloud microphysical properties in tropical convective and stratiform regions. *Meteor. Atmos. Phys.*, **98**, 1–11, https://doi.org/10.1007/s00703-006-0228-1.

Feng, Z., X. Q. Dong, B. K. Xi, C. Schumacher, P. Minnis, and M. Khaiyer, 2011: Top-of-atmosphere radiation budget of convective core/stratiform rain and anvil clouds from deep convective systems. *J. Geophys. Res. Atmos.*, **116**, D23202, https://doi.org/10.1029/2011JD016451.

Gamache, J. F., 1990: Microphysical observations in summer MONEX convective and stratiform clouds. *Mon. Wea. Rev.*, **118**, 1238–1249, https://doi.org/10.1175/1520-0493(1990)118<1238:MOISMC>2.0.CO;2.

Gao, S. T., and X. F. Li, 2010: Precipitation equations and their applications to the analysis of diurnal variation of tropical oceanic rainfall. *J. Geophys. Res. Atmos.*, **115**, D08204, https://doi.org/10.1029/2009jd012452.

Gao, S. T., X. P. Cui, Y. S. Zhou, and X. F. Li, 2005: Surface rainfall processes as simulated in a cloud-resolving model. *J. Geophys. Res. Atmos.*, **110**, D10202, https://doi.org/10.1029/2004jd005467.

Gao, S. T., X. P. Cui, and X. F. Li, 2009: A modeling study of diurnal rainfall variations during the 21-day period of TOGA COARE. *Adv. Atmos. Sci.*, **26**, 895–905, https://doi.org/10.1007/s00376-009-8123-6.

Grim, J. A., G. M. McFarquhar, R. M. Rauber, A. M. Smith, and B. F. Jewett, 2009: Microphysical and thermodynamic structure and evolution of the trailing stratiform regions of mesoscale convective systems during BAMEX. Part II: Column model simulations. *Mon. Wea. Rev.*, **137**, 1186–1205. https://doi.org/10.1175/2008MWR2505.1.

Houze, R. A., Jr., 1977: Structure and dynamics of a tropical squall-line system. *Mon. Wea. Rev.*, **105**, 1540–1567. https://doi.org/10.1175/1520-0493(1977)105<1540:SADOAT>2.0.CO;2.

Houze, R. A., Jr., 1982: Cloud clusters and large-scale vertical motions in the tropics. *J. Meteor. Soc. Japan*, **60**, 396–410, https://doi.org/10.2151/jmsj1965.60.1_396.

Houze, R. A., Jr., 1989: Observed structure of mesoscale convective systems and implications for large-scale heating. *Quart. J. Roy. Meteor. Soc.*, **115**, 425–461, https://doi.org/10.1002/qj.49711548702.

Houze, R. A., Jr., 1997: Stratiform precipitation in regions of convection: A meteorological paradox? *Bull. Amer. Meteor. Soc.*, **78**, 2179–2196, https://doi.org/10.1175/1520-0477(1997)078<2179:SPIROC>2.0.CO;2.

Houze, R. A., Jr., 2014: *Cloud Dynamics*. 2nd ed. Academic Press, 496 pp.

Huang, Y. J., and X. P. Cui, 2015a: Dominant cloud microphysical processes of a torrential rainfall event in Sichuan, China. *Adv. Atmos. Sci.*, **32**, 389–400, https://doi.org/10.1007/s00376-014-4066-7.

Huang, Y. J., and X. P. Cui, 2015b: Moisture sources of torrential rainfall events in the Sichuan basin of China during summers of 2009–13. *Journal of Hydrometeorology*, **16**, 1906–1917, https://doi.org/10.1175/jhm-d-14-0220.1.

Huang, Y. J., X. P. Cui, and Y. P. Wang, 2016a: Cloud micro-

physical differences with precipitation intensity in a torrential rainfall event in Sichuan, China. *Atmospheric and Oceanic Science Letters*, **9**, 90–98, https://doi.org/10.1080/16742834.2016.1139436.

Huang, Y. J, X. P. Cui, and X. F. Li, 2016b: A three-dimensional WRF-based precipitation equation and its application in the analysis of roles of surface evaporation in a torrential rainfall event. *Atmospheric Research*, **169**, 54–64, https://doi.org/10.1016/j.atmosres.2015.09.026.

Huang, Y. J., and Coauthors, 2018: Forecasting severe convective storms with WRF-based RTFDDA radar data assimilation in Guangdong, China. *Atmospheric Research*, **209**, 131–143, https://doi.org/10.1016/j.atmosres.2018.03.010.

Kumar, V. V., A. Protat, C. Jakob, C. R. Williams, S. Rauniyar, G. L. Stephens, and P. T. May, 2016: The estimation of convective mass flux from radar reflectivities. *Journal of Applied Meteorology and Climatology*, **55**, 1239–1257, https://doi.org/10.1175/JAMC-D-15-0193.1.

Li, Q., X. P. Cui, and J. Cao, 2014: Observational analysis and numerical simulation of a heavy rainfall event in Sichuan Province. *Chinese Journal of Atmospheric Sciences*, **38**, 1095–1108, https://doi.org/10.3878/j.issn.1006-9895.1401.13255.

Li, X. F., 2006: Cloud microphysical and precipitation responses to a large-scale forcing in the tropical deep convective regime. *Meteor. Atmos. Phys.*, **94**, 87–102, https://doi.org/10.1007/s00703-005-0172-5.

Luo, Y. L., Y. J. Wang, H. Y. Wang, Y. J. Zheng, and H. Morrison, 2010: Modeling convective-stratiform precipitation processes on a Mei-Yu front with the Weather Research and Forecasting model: Comparison with observations and sensitivity to cloud microphysics parameterizations. *J. Geophys. Res. Atmos.*, **115**, D18117, https://doi.org/10.1029/2010jd013873.

Milbrandt, J. A., and M. K. Yau, 2005a: A multimoment bulk microphysics parameterization. Part I: Analysis of the role of the spectral shape parameter. *J. Atmos. Sci.*, **62**, 3051–3064, https://doi.org/10.1175/Jas3534.1.

Milbrandt, J. A., and M. K. Yau, 2005b: A multimoment bulk microphysics parameterization. Part II: A proposed three-moment closure and scheme description. *J. Atmos. Sci.*, **62**, 3065–3081, https://doi.org/10.1175/Jas3535.1.

Milbrandt, J. A., M. K. Yau, J. Mailhot, S. Bélair, and R. McTaggart-Cowan, 2010: Simulation of an orographic precipitation event during IMPROVE-2. Part II: Sensitivity to the number of moments in the bulk microphysics scheme. *Mon. Wea. Rev.*, **138**, 625–642, https://doi.org/10.1175/2009MWR3121.1.

Morrison, H., G. Thompson, and V. Tatarskii, 2009: Impact of cloud microphysics on the development of trailing stratiform precipitation in a simulated squall line: Comparison of one- and two-moment schemes. *Mon. Wea. Rev.*, **137**, 991–1007, https://doi.org/10.1175/2008mwr2556.1.

Mrowiec, A. A., C. Rio, A. M. Fridlind, A. S. Ackerman, A. D. Del Genio, O. M. Pauluis, A. C. Varble, and J. W. Fan, 2012: Analysis of cloud-resolving simulations of a tropical mesoscale convective system observed during TWP-ICE: Vertical fluxes and draft properties in convective and stratiform regions. *J. Geophys. Res. Atmos.*, **117**, D19201, https://doi.org/10.1029/2012JD017759.

Niu, S. J., X. C. Jia, J. R. Sang, X. L. Liu, C. S. Lu, and Y. G. Liu, 2010: Distributions of raindrop sizes and fall velocities in a semiarid plateau climate: Convective versus stratiform rains. *Journal of Applied Meteorology and Climatology*, **49**, 632–645, https://doi.org/10.1175/2009JAMC2208.1.

Penide, G., V. V. Kumar, A. Protat, and P. T. May, 2013: Statistics of drop size distribution parameters and rain rates for stratiform and convective precipitation during the North Australian Wet Season. *Mon. Wea. Rev.*, **141**, 3222–3237, https://doi.org/10.1175/mwr-d-12-00262.1.

Rapp, A. D., A. G. Peterson, O. W. Frauenfeld, S. M. Quiring, and E. B. Roark, 2014: Climatology of storm characteristics in Costa Rica using the TRMM precipitation radar. *Journal of Hydrometeorology*, **15**, 2615–2633, https://doi.org/10.1175/JHM-D-13-0174.1.

Romatschke, U., and R. A. Houze, Jr., 2011: Characteristics of precipitating convective systems in the South Asian Monsoon. *Journal of Hydrometeorology*, **12**, 3–26, https://doi.org/10.1175/2010JHM1289.1.

Rulfová, Z., and J. Kyselý, 2013: Disaggregating convective and stratiform precipitation from station weather data. *Atmospheric Research*, **134**, 100–115. https://doi.org/10.1016/j.atmosres.2013.07.015.

Sharma, S., M. Konwar, D. K. Sarma, M. C. R. Kalapureddy, and A. R. Jain, 2009: Characteristics of rain integral parameters during tropical convective, transition, and stratiform rain at Gadanki and its application in rain retrieval. *Journal of Applied Meteorology and Climatology*, **48**, 1245–1266, https://doi.org/10.1175/2008JAMC1948.1.

Shen, X. Y., Y. Wang, and X. F. Li, 2011: Effects of vertical wind shear and cloud radiative processes on responses of rainfall to the large-scale forcing during pre-summer heavy rainfall over southern China. *Quart. J. Roy. Meteor. Soc.*, **137**, 236–249, https://doi.org/10.1002/qj.735.

Steiner, M., R. A. Houze Jr., and S. E. Yuter, 1995: Climatological characterization of three-dimensional storm structure from operational radar and rain gauge data. *J. Appl. Meteor.*, **34**, 1978–2007, https://doi.org/10.1175/1520-0450(1995)034<1978:ccotds>2.0.co;2.

Sui, C. H., K. M. Lau, W. K. Tao, and J. Simpson, 1994: The tropical water and energy cycles in a cumulus ensemble model. Part I: Equilibrium climate. *J. Atmos. Sci.*, **51**, 711–728, https://doi.org/10.1175/1520-0469(1994)051<0711:Ttwaec>2.0.Co;2.

Sui, C. H., C. T. Tsay, and X. F. Li, 2007: Convective - stratiform rainfall separation by cloud content. *J. Geophys. Res. Atmos.*, **112**, D14213, https://doi.org/10.1029/2006jd008082.

Tao, W.-K., J. Simpson, C. H. Sui, B. Ferrier, S. Lang, J. Scala, M. D. Chou, and K. Pickering, 1993: Heating, moisture, and water budgets of tropical and midlatitude squall lines: Comparisons and sensitivity to longwave radiation. *J. Atmos. Sci.*, **50**, 673–690, https://doi.org/10.1175/1520-0469(1993)050<0673:HMAWBO>2.0.CO;2.

Tao, W.-K., S. Lang, J. Simpson, W. S. Olson, D. Johnson, B. Ferrier, C. Kummerow, and R. Adler, 2000: Vertical profiles of latent heat release and their retrieval for TOGA COARE convective systems using a cloud resolving model, SSM/I, and ship-borne radar data. *J. Meteor. Soc. Japan*, **78**, 333–355, https://doi.org/10.1175/1520-0450(2001)040<0957:RVPOLH>2.0.CO;2.

Tao, W.-K., S. Lang, X. P. Zeng, S. Shige, and Y. Takayabu, 2010: Relating convective and stratiform rain to latent heating. *J. Climate* **23**, 1874–1893, https://doi.org/10.1175/2009jcli3278.1.

Tao, W.-K., Coauthors, 2001: Retrieved vertical profiles of la-

tent heat release using TRMM rainfall products for February 1998. *J. Appl. Meteor.*, **40**, 957–982, https://doi.org/10.1175/1520-0450(2001)040<0957:RVPOLH>2.0.CO;2.

Thurai, M., P. N. Gatlin, and V. N. Bringi, 2016: Separating stratiform and convective rain types based on the drop size distribution characteristics using 2D video disdrometer data. *Atmospheric Research.*, **169**, 416–423, https://doi.org/10.1016/j.atmosres.2015.04.011.

Wang, D. H., X. F. Li, and W.-K. Tao, 2010: Cloud radiative effects on responses of rainfall to large-scale forcing during a landfall of severe tropical storm Bilis (2006). *Atmospheric Research*, **98**, 512–525, https://doi.org/10.1016/j.atmosres.2010.08.020.

Wang, J. J., X. F. Li, and L. D. Carey, 2007: Evolution, structure, cloud microphysical, and surface rainfall processes of monsoon convection during the South China Sea monsoon experiment. *J. Atmos. Sci.*, **64**, 360–380, https://doi.org/10.1175/jas3852.1.

Wu, D., X. Q. Dong, B. K. Xi, Z. Feng, A. Kennedy, G. Mullendore, M. Gilmore, and W. K. Tao, 2013: Impacts of microphysical scheme on convective and stratiform characteristics in two high precipitation squall line events. *J. Geophys. Res. Atmos.*, **118**, 11 119–111 135, https://doi.org/10.1002/jgrd.50798.

Xu, K. M., 1995: Partitioning mass, heat, and moisture budgets of explicitly simulated cumulus ensembles into convective and stratiform components. *J. Atmos. Sci.*, **52**, 551–573, https://doi.org/10.1175/1520-0469(1995)052<0551:Pmhamb>2.0.Co;2.

Yang, S., and E. A. Smith, 2000: Vertical structure and transient behavior of convective-stratiform heating in TOGA COARE from combined satellite-sounding analysis. *J. Appl. Meteor.*, **39**, 1491–1513, https://doi.org/10.1175/1520-0450(2000)039<1491:VSATBO>2.0.CO;2.

Yang, Y., X. Chen, and Y. C. Qi, 2013: Classification of convective/stratiform echoes in radar reflectivity observations using a fuzzy logic algorithm. *J. Geophys. Res. Atmos.*, **118**, 1896–1905, https://doi.org/10.1002/jgrd.50214.

Yuter, S. E., and R. A. Houze Jr., 1995: Three-dimensional kinematic and microphysical evolution of Florida cumulonimbus. Part II: Frequency distributions of vertical velocity, reflectivity, and differential reflectivity. *Mon. Wea. Rev.*, **123**, 1941–1963, https://doi.org/10.1175/1520-0493(1995)123<1941:TDKAME>2.0.CO;2.

Zipser, E. J., 1977: Mesoscale and convective–scale downdrafts as distinct components of squall-line structure. *Mon. Wea. Rev.*, **105**, 1568–1589, https://doi.org/10.1175/1520-0493(1977)105<1568:MACDAD>2.0.CO;2.